Journal of
Applied
Crystallography
ISSN 0021-8898

Received 14 August 2006
Accepted 20 October 2006

© 2007 International Union of Crystallography
Printed in Great Britain – all rights reserved

GISAXS study of cavities and {113} defects induced by neon and helium implantation in silicon

David Babonneau,[a]* Suzana Peripolli,[a,b] Marie-France Beaufort,[a] Jean-François Barbot[a] and Jean-Paul Simon[c]

[a]Laboratoire de Métallurgie Physique, UMR 6630 CNRS- Université de Poitiers, SP2MI, Téléport 2, Boulevard Marie et Pierre Curie, BP 30179, 86962 Futuroscope Chasseneuil Cedex, France, [b]Instituto de Física, Universidade Federal do Rio Grande do Sul, Avenida Bento Gonçalves, 9500, CP 15051, 91501-970 Porto Alegre, RS, Brazil, and [c]Laboratoire de Thermodynamique et Physicochimie Métallurgiques, UMR 5614 CNRS-INPG-UJF, 1130 rue de la Piscine, BP 75, 38402 Saint-Martin d'Hères Cedex, France. Correspondence e-mail: david.babonneau@univ-poitiers.fr

Grazing incidence small-angle X-ray scattering experiments have been performed to study the morphology of nanocavities and {113} defects formed by implantation of 5×10^{16} cm^{-2} neon and helium ions in Si(001) at 50 keV. The results show that spherical cavities are formed in Si(001) implanted with Ne ions at 873 K and in Si(001) implanted with He ions at 473 K subsequently annealed at 873 K. In contrast, He-induced cavities at 873 K show {111} facets and wide size distribution due to an enhanced He mobility at high temperature. In addition to the faceted cavities, the clustering of interstitials leads to the formation of large extended planar {113} defects whose size has been estimated to be about 100 nm.

1. Introduction

Helium implantation in crystalline silicon leads to the formation of peculiar defective nanostructures such as bubbles, *i.e.* gas-filled cavities. Upon annealing, bubbles coarsen and degas leaving voids, *i.e.* empty cavities (Griffioen *et al.*, 1987). Cavities in the Si(He) system have received considerable attention in the last decade due to the binding of metal atoms on their surface, which can be used for impurity gettering in microelectronic devices (Follstaedt *et al.*, 1996). Simultaneously to the formation of cavities, stable extended interstitials-type defects can appear (Oliviero *et al.*, 2000; Beaufort *et al.*, 2000). The morphological characteristics of these nanostructures, which are located around the ion-peak concentration (R_p), are strongly dependent on the implantation parameters (energy, fluence, temperature). Thus a lot of fundamental studies have been reported and the basic mechanisms involved in the growth of the cavities has been much discussed (Frabboni *et al.*, 2004). In addition strong efforts have been carried out to investigate the evolution of the so-called {113} defects, which are the most important extended defects formed in He-implanted Si (David *et al.*, 2003; da Silva *et al.*, 2004; Beaufort *et al.*, 2006). On the other hand, the formation of cavities by using other gases is studied to obtain more fundamental data on their growth mechanisms and to lower the budgets for their integration in advanced circuits. Implantation of neon at elevated temperature is particularly interesting due to the high activation energy for permeation (Cima *et al.*, 2000; Oliviero *et al.*, 2006).

Transmission electron microscopy (TEM) is the main technique used to characterize cavities and extended defects induced by inert-gas implantation in Si with the great advantage of a direct observation (Frabboni *et al.*, 2004). However, TEM provides a local image (two-dimensional) which results from nanostructures dispersed in a volume (three-dimensional). Recently, grazing-incidence small-angle X-ray scattering (GISAXS) using synchrotron radiation has been shown to be an alternative and complementary tool for the study of nanostructured thin films (Levine *et al.*, 1989; Naudon & Thiaudière, 1997) as well as ion-implanted materials (Babonneau *et al.*, 2000; Cattaruzza *et al.*, 2000). GISAXS has also been applied successfully to characterize inert-gas-implanted Si (Dubček *et al.*, 2000, 2004; Babonneau *et al.*, 2006) as the technique is sensitive to the electron density modulation obtained in a non-destructive way and averaged over a large amount of material. Thus, it has been demonstrated that useful information on the size, shape, and depth profile of both the cavities and {113} defects can be obtained from the quantitative analysis of the two-dimensional GISAXS data (Babonneau *et al.*, 2006).

In this paper we present a GISAXS study of nanostructures induced by neon and helium implantation in silicon. The morphological dependences of the cavities and {113} defects upon the nature of the implanted ions are investigated.

2. Experimental procedure

Ne^+ and He^+ ions with an energy of 50 keV and a fluence of 5×10^{16} cm^{-2} were implanted into (001) silicon substrates at 873 K. An additional sample was implanted with 5×10^{16} He^+ cm^{-2} at 473 K and subsequently annealed at 873 K. Fig. 1 shows the atomic concentration profiles of Ne and He determined from SRIM 2003 calculations (Ziegler & Biersack, 2003). They predict a Ne-peak concentration of 8.7 at.% with a mean projected range $R_p = 110$ nm and a straggling $\Delta R_p = 43$ nm. Similarly, an He-peak concentration of 4.3 at.% with $R_p = 417$ nm and $\Delta R_p = 105$ nm is predicted.

GISAXS experiments were performed at the European Synchrotron Radiation Facility on the D2AM beamline. The sample surface was illuminated under vacuum with a highly collimated X-ray beam of wavelength $\lambda = 0.139$ nm at a grazing angle $\alpha_i = 0.4°$, so that the penetration depth of the incident X-ray beam was $z_{1/e} = 584$ nm (Fig. 1). The transmitted and specularly reflected beams were masked by a

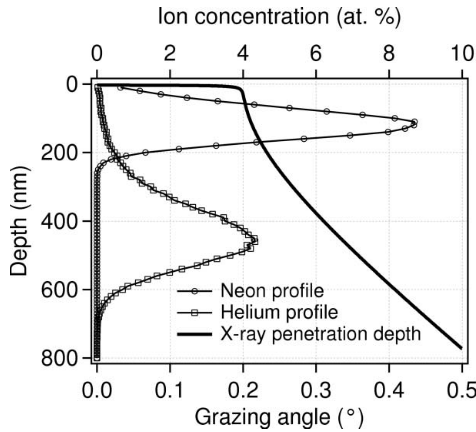

Figure 1
Atomic concentration profile of Ne and He as determined by SRIM calculations (Ziegler & Biersack, 2003) for 5×10^{16} ions cm^{-2} implanted in Si at 50 keV. The variation of the penetration depth [equation (4)] of the incident X-ray beam in Si at $\lambda = 0.139$ nm is also shown as a function of the grazing angle.

vertical beam-stop. The scattering intensity was collected for different azimuthal positions ψ with a two-dimensional charge-coupled device (CCD) detector placed at 570 mm from the sample. Before quantitative analysis, raw data were corrected for the background and non-uniform sensitivity of the CCD.

3. GISAXS theory applied to implanted materials

In order to calculate the scattering intensity for implanted materials, we consider an X-ray beam impinging on the surface ($z = 0$) of a semi-infinite and homogeneous medium. In the grazing incidence geometry, the incident and scattered waves in vacuum are described by wavevectors $\mathbf{k}^i$ and $\mathbf{k}^f$, which are defined by the in-plane and out-of-plane angles $(2\theta_i, \alpha_i)$ and $(2\theta_f, \alpha_f)$, respectively. The scattering vector in vacuum $\mathbf{q} = (\mathbf{q_y}, \mathbf{q_z})$ ($q_x \approx 0$) is then defined by

$$\mathbf{q} = \mathbf{k}^f - \mathbf{k}^i = \frac{2\pi}{\lambda}\begin{bmatrix} \sin(2\theta_f)\cos(\alpha_f) \\ \sin(\alpha_f) + \sin(\alpha_i) \end{bmatrix}. \quad (1)$$

For hard X-rays, the refractive index n of the medium is complex and can be written (Parratt, 1954),

$$n = 1 - \delta - i\beta \quad (2)$$

with a dispersion term $\delta = 6.12 \times 10^{-6}$ and an absorption term $\beta = 1.14 \times 10^{-7}$ for Si at $\lambda = 0.139$ nm. In this condition the refracted beam propagates within the implanted material with an exponentially damped wave described by a wavevector $\widetilde{\mathbf{k}}^i$. The scattering vector in the medium $\widetilde{\mathbf{q}} = (\widetilde{q}_y, \widetilde{q}_z)$ is complex and defined by

$$\widetilde{\mathbf{q}} = \frac{2\pi}{\lambda}\begin{bmatrix} \sin(2\theta_f)\cos(\alpha_f) \\ \sqrt{n^2 - \cos^2(\alpha_f)} + \sqrt{n^2 - \cos^2(\alpha_i)} \end{bmatrix}, \quad (3)$$

and the penetration depth $z_{1/e} = f(\alpha_i)$ at which the intensity is reduced to $1/e$ is given by (Parratt, 1954),

$$z_{1/e}(\alpha_i) = \frac{\lambda\sqrt{2}}{4\pi}\left[\sqrt{\left(\alpha_i^2 - 2\delta\right)^2 + 4\beta^2} - \alpha_i^2 + 2\delta\right]^{-\frac{1}{2}}. \quad (4)$$

Thus the scattering intensity (corrected for refraction and for absorption within the medium) originating from of an object located at a depth z from the surface can be expressed by

$$I\left(q_y, q_z\right) \propto \left|T(\alpha_i)\right|^2 \left|T\left(\alpha_f\right)\right|^2 \left|F\left(\widetilde{q}_y, \widetilde{q}_z\right)\right|^2 \exp\left(-\frac{z}{z_0}\right), \quad (5)$$

where $F(\widetilde{q}_y, \widetilde{q}_z)$ is the form factor of the scattering object, $T(\alpha_i)$ and $T(\alpha_f)$ are the Fresnel transmission coefficients in incidence and emergence, respectively,

$$T(\alpha_{i,f}) = \frac{2k_z^{i,f}}{k_z^{i,f} + \widetilde{k}_z^{i,f}}, \quad (6)$$

and

$$\frac{1}{z_0} = \frac{1}{z_{1/e}(\alpha_i)} + \frac{1}{z_{1/e}\left(\alpha_f\right)}. \quad (7)$$

To calculate the total scattering intensity $I_{\rm tot}(q_y, q_z)$, we now consider that all the scattering bodies are randomly distributed within the implanted material between $z = R_{\rm p} - \Delta R_{\rm p}$ and $z = R_{\rm p} + \Delta R_{\rm p}$,

$$I_{\rm tot}\left(q_y, q_z\right) \propto |T(\alpha_i)|^2 |T(\alpha_f)|^2 \int_0^\infty |F(\widetilde{q}_y, \widetilde{q}_z)|^2 N(D) {\rm d}D \times \int_{R_{\rm p}-\Delta R_{\rm p}}^{R_{\rm p}+\Delta R_{\rm p}} \exp\left(-\frac{z}{z_0}\right) {\rm d}z \Bigg/ \int_{R_{\rm p}-\Delta R_{\rm p}}^{R_{\rm p}+\Delta R_{\rm p}} {\rm d}z, \quad (8)$$

where $N(D)$ represents the size distribution of the scattering bodies. Thus, from equation (8), the total scattering intensity measured in an experiment can be calculated as

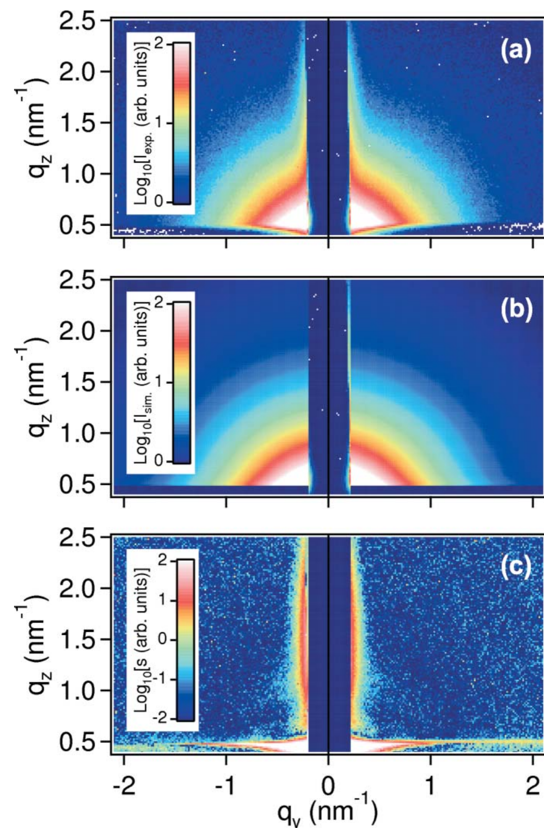

Figure 2
(*a*) Two-dimensional experimental GISAXS pattern of Si(001) Ne-implanted at 873 K with the incident beam along the Si[110] direction. (*b*) Two-dimensional simulated GISAXS pattern assuming a log-normal distribution of spherical cavities with $D_m = 10.1$ nm and $W = 7.6$ nm. (*c*) Two-dimensional error signal defined by $s(q_y, q_z) = \left[I_{\rm exp}(q_y, q_z) - I_{\rm sim}(q_y, q_z)\right]^2 / I_{\rm sim}(q_y, q_z)$.

$$I_{\rm tot}(q_y,q_z)\propto |T(\alpha_i)|^2|T(\alpha_f)|^2\int_0^\infty |F(\widetilde{q}_y,\widetilde{q}_z)|^2 N(D){\rm d}D \times\frac{z_0}{2\Delta R_{\rm p}}\left[\exp\left(-\frac{R_{\rm p}-\Delta R_{\rm p}}{z_0}\right)-\exp\left(-\frac{R_{\rm p}+\Delta R_{\rm p}}{z_0}\right)\right]. \tag{9}$$

4. Results and discussion

4.1. GISAXS from Ne-implanted Si(001)

Fig. 2(*a*) shows the two-dimensional experimental GISAXS pattern of the Ne-implanted sample at 873 K with the incident beam along the Si[110] direction. The two-dimensional GISAXS pattern exhibits an isotropic scattering signal without interference maximum. Furthermore, GISAXS measurements performed for azimuthal positions ranging from $\psi = 0$ to 90° show no evidence of in-plane anisotropy. Therefore the GISAXS signal can be ascribed to spherical cavities randomly distributed within the cavity-rich region of the implanted material. Thus the form factor of a sphere [see equation (12) in Appendix A] was used in equation (9) for the quantitative analysis of the two-dimensional experimental data, assuming a log-normal distribution function defined by

$$N(D)=\frac{1}{D\ln\sigma\sqrt{2\pi}}\exp\left[-\frac{(\ln D-\ln\overline{D})^2}{2(\ln\sigma)^2}\right], \tag{10}$$

where D is the cavity diameter. The parameters $\overline{D}$ and σ, which denote the statistical median of the distribution and the geometric standard deviation, respectively, are related to the average diameter D_m and the full width at half-maximum W by

$$D_m=\overline{D}\exp\left[\frac{3}{2}\left(\ln\sigma\right)^2\right] \text{ and } W=2\overline{D}\sinh(\ln\sigma\sqrt{2\ln 2}). \tag{11}$$

The GISAXS formalism described above was applied to fit the two-dimensional experimental pattern by using the Levenberg–Marquadt algorithm (Press *et al.*, 1992) to determine the parameter values of D_m and W that minimize χ^2. Fig. 2(*b*) displays the two-dimensional simulated pattern with $D_m = 10.1$ nm and $W = 7.6$ nm. The associated error signal defined by $s(q_y, q_z) = [I_{\rm exp}(q_y, q_z) - I_{\rm sim}(q_y, q_z)]^2/I_{\rm sim}(q_y, q_z)$ is presented in Fig. 2(*c*). The agreement between the two-dimensional experimental and simulated data is very satisfactory except in the zone close to the beam-stop, which contains information about the surface roughness and large scale structures. It is worth noting that these results are consistent with TEM observations (Fig. 3), which confirm the spherical shape of the majority of the observed cavities (Peripolli *et al.*, 2005). However, TEM experiments enable different regions to be distinguished: in the near surface region ($z < R_{\rm p} - \Delta R_{\rm p}$) the cavities are rather small, a few nanometres in diameter, whereas close to the end of the band ($z > R_{\rm p}$) their diameter can reach 15 nm. This is in agreement with the large value of W calculated from GISAXS experiments as the depth distribution $N(z)$ of the cavities is not included in the model. Beyond the cavity band ($z > R_{\rm p} + \Delta R_{\rm p}$), {113} defects of approximately 15 nm in width are also observed by TEM (Fig. 3). As seen in Fig. 2(*a*), they do not induce any scattering signal in the two-dimensional experimental GISAXS pattern. At this stage, one can argue that their contribution is hidden by the strong scattering intensity of the cavities because of combining effects (low {113} defect density, small size, deep location).

4.2. GISAXS from He-implanted Si(001)

Figs. 4 and 5 show the two-dimensional experimental and simulated GISAXS patterns of the He-implanted sample at 873 K for azimuthal positions $\psi = 0°$ and $\psi = 26.57°$, respectively, corresponding to Si[110] and Si[310] directions. It should be noted that similar results are obtained with $\psi = 90°$ and $\psi = 63.43°$ corresponding to Si[1$\bar{1}$0] and Si[3$\bar{1}$0] directions, respectively. The two-dimensional GISAXS patterns present enlarged streaks at 54.7° with respect to the surface normal whenever the incident beam is along ⟨110⟩ directions. This indicates that He-induced cavities form {111} facets as already shown in low-fluence He-implanted Si (Babonneau *et al.*, 2006). In addition, sharp rods at 25.2° with respect to the surface normal appear in the

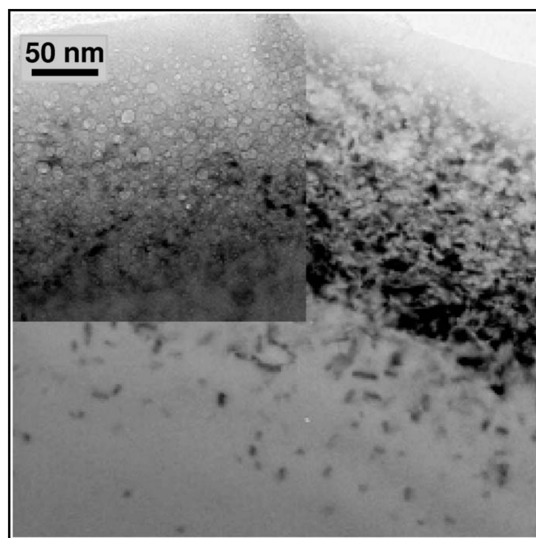

Figure 3
Cross-sectional TEM bright field micrograph of the Ne-implanted sample at 873 K (cavities can be clearly seen as white spot with a dark edge for underfocus conditions in the inset).

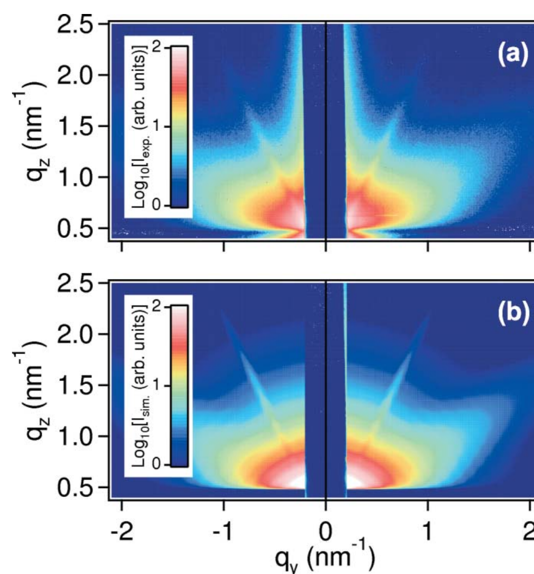

Figure 4
(*a*) Two-dimensional experimental GISAXS pattern of Si(001) He-implanted at 873 K with the incident beam along the Si[110] direction. (*b*) Two-dimensional simulated GISAXS pattern assuming a log-normal distribution of {111} faceted cavities associated with elongated {113} defects.

two-dimensional GISAXS patterns recorded in the ⟨110⟩ directions. Although strongly attenuated, similar rods also appear at 72.5° with respect to the surface normal in the two-dimensional GISAXS patterns recorded in the ⟨310⟩ directions. This suggests that elongated {113} defects are present in the He-implanted sample at 873 K.

The two-dimensional experimental patterns were analyzed assuming cavities with a faceted sphere-like average shape and {113} defects with a disk-like shape [see equations (13) and (14) in Appendix A]. All the possible orientations were taken into account in the calculation of the two-dimensional simulated patterns, *i.e.*, 4 equiprobable orientations for the {111} faceted cavities and 12 equiprobable orientations for the {113} defects. Furthermore, a shape distribution as determined by Babonneau *et al.* (2006) was introduced in the fit procedure to describe the size-dependent shape anisotropy of the cavities. Within the framework of these assumptions, the best fit was obtained using a log-normal distribution of {111} faceted cavities with $D_m = 20.1$ nm and $W = 26.7$ nm associated with elongated {113} defects of average width 100 nm and average thickness 2 nm. The simulated GISAXS patterns in Figs. 4(*b*) and 5(*b*) reproduce the general features of the experimental patterns well both in the ⟨110⟩ and ⟨310⟩ directions. One can also notice that the GISAXS intensity from {113} defects in the ⟨310⟩ directions is very weak, which is consistent with our experimental observations.

Helium implantation at 873 K leads to the formation of faceted cavities and of large {113} defects. In contrast, GISAXS measurements from Si(001) implanted with He ions at 473 K and post-annealed at 873 K (Fig. 6) show a scattering signal very similar to that of Si(001) implanted with Ne ions at 873 K (Fig. 2). The quantitative analysis of the GISAXS intensity in Fig. 6 yields $D_m = 5.3$ nm and $W = 3.0$ nm by assuming a log-normal distribution of spherical cavities in equation (9). It is known that the formation of bubbles in room temperature He-implanted silicon results from the interactions of helium with vacancy-type defects while the self-interstitials can migrate to the surface or be trapped in defect clusters. The defect production and the helium mobility being strongly dependent on the temperature, changes in implant temperature should thus modified the formation of both bubbles and interstitials-type defects. During helium implantation at high temperature (> 573 K), vacancy-type defects can agglomerate and/or coarsen to evolve into larger faceted voids. In addition, helium atoms escape from the sample and only 0.02% of implanted helium has been found to remain in the matrix at 873 K (Oliviero *et al.*, 2002). Simultaneously the clustering and growing of interstitials is enhanced and large stable {113} defects are formed (David *et al.*, 2004).

In contrast, in the Si(Ne) system, the as-induced cavities are found to be spherical even for implantation temperatures as high as 873 K [Fig. 2(*a*)]. Since Ne atoms do not permeate during implantation at 873 K, we can conclude that the retention of neon slows down the surface energy minimization process impeding any bubbles faceting. GISAXS experiments and TEM observations both confirm that only small {113} defects are generated by the high temperature implant whereas neon ions produce five times more Frenkel pairs than helium ions. Therefore, the implanted gas is also supposed to play a role in the formation and evolution of such defects. The mobility of neon atoms being supposed to be lower than that of helium, the dissolution and migration of small interstitial clusters to form large {113} defects is impeded.

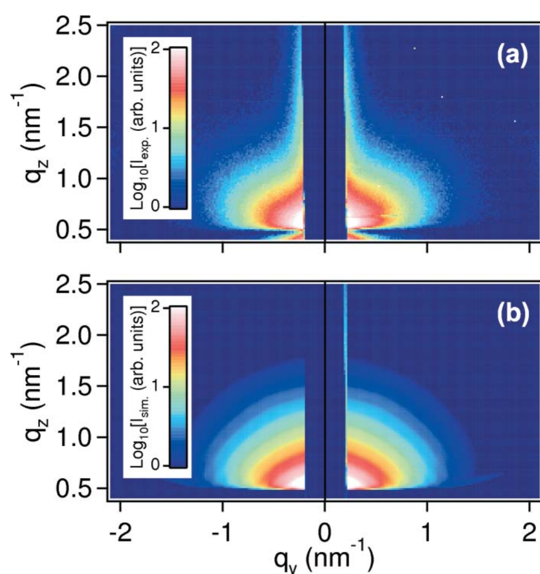

Figure 5
(*a*) Two-dimensional experimental GISAXS pattern of Si(001) He-implanted at 873 K with the incident beam along the Si[310] direction. (*b*) Two-dimensional simulated GISAXS pattern assuming a log-normal distribution of {111} faceted cavities associated with elongated {113} defects.

5. Conclusion

Nondestructive GISAXS measurements have been used to investigate the morphology of nanocavities and {113} defects formed by implantation of Ne and He ions in Si(001). The quantitative analysis of the GISAXS intensity shows that Ne-induced cavities at 873 K and He-induced cavities at 473 K subsequently annealed at 873 K are spherical with average diameter in the 3–17 nm range (respectively 3–7 nm). Furthermore, due to their small size, low density and/or high depth location, the formation of {113} defects has not been evidenced in these cases. In contrast, GISAXS measurements of He-implanted Si at 873 K clearly show the formation of both {111} faceted cavities with wide size distribution and large {113} planar defects with an average width of about 100 nm and a thickness around 2 nm. These results confirm that the mobility of the ions and interstitials is a key parameter in the formation and evolution of defects created in implanted materials.

APPENDIX *A*
The form factor expressions

The GISAXS intensity was fitted with the following expressions for the form factors (Guinier & Fournet, 1955; Babonneau *et al.*, 2006):

Full sphere with radius R:

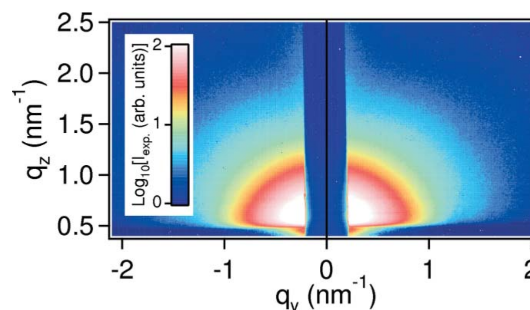

Figure 6
Two-dimensional experimental GISAXS pattern of Si(001) He-implanted at 473 K and post-annealed at 873 K.

$$F(q_x, q_y, q_z) = 4\pi R^3 \frac{\sin(qR) - qR\cos(qR)}{(qR)^3}, \qquad (12)$$

with $q = \sqrt{q_x^2 + q_y^2 + q_z^2}$.

Faceted sphere with radius R and height H:

$$F(q_x, q_y, q_z) = \int_0^{H/2} 4\pi R_z^2 \frac{J_1(q_\parallel R_z)}{q_\parallel R_z} \cos(q_z z) \mathrm{d}z \qquad (13)$$

with $q_\parallel = \sqrt{q_x^2 + q_y^2}$ and $R_z = \sqrt{R^2 - z^2}$.

Disk with radius R and height H:

$$F(q_x, q_y, q_z) = 2\pi R^2 H \frac{J_1(q_\parallel R)}{q_\parallel R} \mathrm{sin}_c\left(\frac{q_z H}{2}\right), \qquad (14)$$

with $q_\parallel = \sqrt{q_x^2 + q_y^2}$.

We would like to thank M. Marteau for performing the implantation experiments and all the staff of the CRG-D2AM beamline for their assistance during the GISAXS measurements. We also wish to thank the program CAPES-COFECUB for financial support.

References

Babonneau, D., Beaufort, M. F., Declémy, A., Barbot J. F. & Simon, J. P. (2006). *J. Appl. Phys.* **99**, 113507/1–6.

Babonneau, D., Naudon, A., Cabio'ch, T. & Lyon, O. (2000). *J. Appl. Cryst.* **33**, 437–441.

Beaufort, M. F., Donnelly, S. E., Rousselet, S., David, M. L. & Barbot, J. F. (2006). *Nucl. Instrum. Methods Phys. Res. B*, **242**, 565–567.

Beaufort, M. F., Oliviero, E., Garem, H., Godey, S., Ntsoenzok, E., Blanchard, C. & Barbot, J. F. (2000). *Philos. Mag. B*, **80**, 1975–1985.

Cattaruzza, E., d'Acapito, F., Gonella, F., Longo, A., Martonara, A., Mattei, G., Maurizio, C. & Thiaudiere, D. (2000). *J. Appl. Cryst.* **33**, 740–743.

Cima, C. A., Boudinov, H., de Souza, J. P., Suprun-Belevich, Yu. & Fichtner, P. F. P. (2000). *J. Appl. Phys.* **88**, 1171–1175.

David, M. L., Beaufort, M. F. & Barbot, J. F. (2003). *J. Appl. Phys.* **93**, 1438–1442.

David, M. L., Beaufort, M. F. & Barbot, J. F. (2004). *Nucl. Instrum. Methods Phys. Res. B*, **226**, 531–536.

Dubček, P., Milat, O., Pivac, B., Bernstorff, S., Amenitsch, H., Tonini, R., Corni, F. & Ottaviani, G. (2000). *Mater. Sci. Eng. B*, **71**, 82–86.

Dubček, P., Pivac, B., Milat, O., Bernstorff, & Zulim, I. (2004). *Nucl. Instrum. Methods Phys. Res. B*, **215**, 122–128.

Follstaedt, D. M., Myers, S. M., Petersen, G. A. & Medernach, J. W. (1996). *J. Electron. Mater.* **25**, 157–170.

Frabboni, S., Corni, F., Nobili, C., Tonini, R. & Ottaviani, G. (2004). *Phys. Rev. B*, **69**, 165209/1–5.

Griffioen, C. C., Evans, J. H., De Jong, P. C. & Van Veen, A. (1987). *Nucl. Instrum. Methods Phys. Res. B*, **27**, 417–420.

Guinier, A. & Fournet, G. (1955). *Small-Angle Scattering of X-rays*. New York: John Wiley.

Levine, J. R., Cohen, J. B., Chung, Y. W. & Georgopoulos, P. (1989). *J. Appl. Cryst.* **22**, 528–532.

Naudon, A. & Thiaudière, D. (1997). *J. Appl. Cryst.* **30**, 822–827.

Oliviero, E., Beaufort, M. F. & Barbot, J. F. (2000). *J. Appl. Phys.* **89**, 5332–5338.

Oliviero, E., David, M. L., Beaufort, M. F., Barbot, J. F. & van Veen, A. (2002). *Appl. Phys. Lett.* **81**, 4201–4203.

Oliviero, E., Peripolli, S., Amaral, L., Fichtner, P. F. P., Beaufort, M. F., Barbot, J. F. & Donnelly, S. E. (2006). *J. Appl. Phys.* **100**, 043505/1–10.

Parratt, L. G. (1954). *Phys. Rev.* **95**, 359–369.

Peripolli, S., Beaufort, M. F., Babonneau, D., Rousselet, S, Fichtner, P. F. P., Amaral, L., Oliviero, E., Barbot J. F. & Donnelly, S. E. (2005). *Solid State Phenom.*, **108–109**, 357–361.

Press, W. H., Flannery, B. P., Teukolski, S. A. & Vetterling, W. T. (1992). *Numerical Recipes in C*, 2nd ed. Cambridge University Press.

Silva, D. L. da, Mörschbächer, M. J., Fichtner, P. F. P., Oliviero, E. & Behar, M. (2004). *Nucl. Instrum. Methods Phys. Res. B*, **219–220**, 713–717.

Ziegler, J. F. & Biersak J. P. (2003). http://www.srim.Org/.